

Spectral statistics and wave-chaos transition in three-dimensional acoustic cavities

Xiaodong Zhang(张晓东)

Citation: Chin. Phys. B, 2026, 35 (**6**): 060510. DOI: 10.1088/1674-1056/ae3555
http://cpb.iphy.ac.cn; http://iopscience.iop.org/cpb

What follows is a list of articles you may be interested in

Experimental test of an extension of the Rosenzweig-Porter model to mixed integrable-chaotic systems experiencing time-reversal invariance violation

Xiaodong Zhang(张晓东), Jiongning Che(车炯宁), and Barbara Dietz
Chin. Phys. B, 2024, 33 (**12**): 120501. DOI: 10.1088/1674-1056/ad8a4e

Dynamical localization in a non-Hermitian Floquet synthetic system

Han Ke(可汗), Jiaming Zhang(张嘉明), Liang Huo(霍良), and Wen-Lei Zhao(赵文垒)
Chin. Phys. B, 2024, 33 (**5**): 050507. DOI: 10.1088/1674-1056/ad36bb

Accelerator-mode islands and superdiffusion in double-kicked rotor

Fengdi Wang(王风涤) and Ping Fang(方萍)
Chin. Phys. B, 2023, 32 (**6**): 060504. DOI: 10.1088/1674-1056/accb4b

A novel algorithm to analyze the dynamics of digital chaotic maps in finite-precision domain

Chunlei Fan(范春雷) and Qun Ding(丁群)
Chin. Phys. B, 2023, 32 (**1**): 010501. DOI: 10.1088/1674-1056/ac785c

Experimental investigation of the fluctuations in nonchaotic scattering in microwave billiards

Runzu Zhang(张润祖), Weihua Zhang(张为华), Barbara Dietz, Guozhi Chai(柴国志), Liang Huang(黄亮)
Chin. Phys. B, 2019, 28 (**10**): 100502. DOI: 10.1088/1674-1056/ab3f96

Spectral statistics and wave-chaos transition in three-dimensional acoustic cavities

Xiaodong Zhang(张晓东)[1,2,†]

[1] *Shandong Key Laboratory of Space Environment and Exploration Technology, College of Physics and Electronic Engineering, Qilu Normal University, Jinan* 250200, *China*

[2] *Lanzhou Center for Theoretical Physics, Key Laboratory of Theoretical Physics of Gansu Province, Key Laboratory of Quantum Theory and Applications of MoE, Lanzhou University, Lanzhou* 730000, *China*

(Received 13 November 2025; revised manuscript received 21 December 2025; accepted manuscript online 8 January 2026)

We numerically study three-dimensional acoustic cavities with progressively increasing geometric complexity and analyze their spectral and spatial statistics. The eigenfrequency spectra and adjacent level-spacing ratios reveal a clear transition from Poisson to Gaussian orthogonal ensemble (GOE) statistics as the cavity structure becomes more irregular. The intermediate regimes are quantitatively characterized using the Berry–Robnik (BR) and Brody distributions, which yield consistent estimates of the chaotic fraction. Furthermore, both the participation ratio and long-range spectral correlations confirm the continuous evolution from integrable to chaotic dynamics. The distributions of normalized wavefunction amplitudes gradually approach the Gaussian prediction, indicating the onset of wave chaos. These results demonstrate that three-dimensional acoustic resonators provide a numerically controllable and experimentally accessible platform for studying the universal transition from Poisson to GOE statistics and for exploring the interplay between geometry and wave chaos.

Keywords: wave chaos, spectral statistics, acoustic resonators, Poisson–GOE transition

PACS: 05.45.Mt, 05.45.Pq, 05.45.–a

DOI: 10.1088/1674-1056/ae3555 **CSTR:** 32038.14.CPB.ae3555

1. Introduction

Wave chaos — the study of irregular wave phenomena arising in systems whose classical counterparts exhibit chaotic dynamics — has become a central theme in the exploration of universality across quantum, electromagnetic, and acoustic domains.[1–4] A key manifestation of wave chaos lies in the statistical properties of energy levels and field intensities, which often display remarkable agreement with predictions from random-matrix theory (RMT).[5,6] In the limit of completely integrable dynamics, level spacings follow Poisson statistics, whereas in fully chaotic systems they obey the Wigner–Dyson distributions corresponding to the Gaussian orthogonal or unitary ensembles (GOE/GUE).[5,7] The transition between these two limits encodes the onset of chaotic behavior and has been widely investigated as a signature of mixed regular–chaotic dynamics.[8–11]

Experimental realizations of wave-chaotic systems have been achieved in various physical settings, including microwave and optical resonators, vibrating plates, and elastic or acoustic cavities.[12–16] Microwave billiards[17–19] in particular have provided precise analogs of quantum systems, enabling direct observation of universal spectral statistics, time-reversal symmetry breaking, and scarring phenomena.[1,17,20] Acoustic and elastic resonators, on the other hand, offer a complementary platform where the interplay between geometry, boundary conditions, and material properties can be explored in a macroscopic and experimentally accessible regime. Despite this versatility, most studies have focused on two-dimensional geometries or simple three-dimensional enclosures with limited control over interior complexity.[21,22]

In realistic cavities, irregular boundaries and internal scatterers can strongly affect the propagation of acoustic waves, giving rise to complex modal patterns and long-range correlations. Understanding how geometrical complexity influences the spectral and spatial statistics of acoustic modes is therefore essential for connecting the macroscopic behavior of reverberant environments with the microscopic mechanisms of wave chaos. Moreover, acoustic systems constitute a natural testbed for semiclassical concepts such as periodic-orbit corrections and the correspondence between ray dynamics and spectral fluctuations.[23]

In this work, we perform a comprehensive numerical study of three-dimensional acoustic cavities with progressively increasing geometric complexity. Using finite-element simulations, we compute extensive sets of eigenfrequencies and eigenmodes, and analyze their statistical properties over a broad frequency range. We demonstrate a clear transition from Poisson to GOE statistics in both short- and long-range spectral measures, accompanied by the emergence of Gaussian amplitude statistics and speckle-like mode patterns in space. Furthermore, by isolating the influence of short periodic or-

†Corresponding author. E-mail: xiaodongzhang2021@gmail.com

© 2026 Chinese Physical Society and IOP Publishing Ltd. All rights, including for text and data mining, AI training, and similar technologies, are reserved.

bits through a dedicated filtering scheme, we establish a direct connection between semiclassical orbit dynamics and random-matrix universality.

The remainder of this paper is organized as follows. Section 2 describes the numerical model and eigenfrequency computations. Section 3 presents the statistical analysis of the spectra, highlighting the gradual transition toward universal GOE behavior. Section 4 discusses the spatial statistics of acoustic modes and their correspondence to wave-chaotic features. Appendix A outlines the procedure used to remove periodic-orbit contributions, and Appendix B compares the results obtained with the BR and Brody models.[6,24,25]

2. Numerical model and eigenfrequency computation

The system under study consists of a series of three-dimensional acoustic cavities with progressively increased geometric complexity, as illustrated in Fig. 1. Each cavity is enclosed in a rectangular box of fixed outer dimensions 480 cm×400 cm×250 cm. Within this volume, scatterers and wall indentations are introduced to tune the degree of geometric irregularity, thereby enabling a systematic exploration of how structural complexity influences spectral statistics. Four geometries, labeled (a)–(d), are considered, ranging from a simple rectangular cavity to a highly irregular enclosure containing multiple protrusions and recesses. The total volume of all models is kept constant so that any variation in spectral or spatial statistics arises solely from geometric complexity rather than from scaling effects.

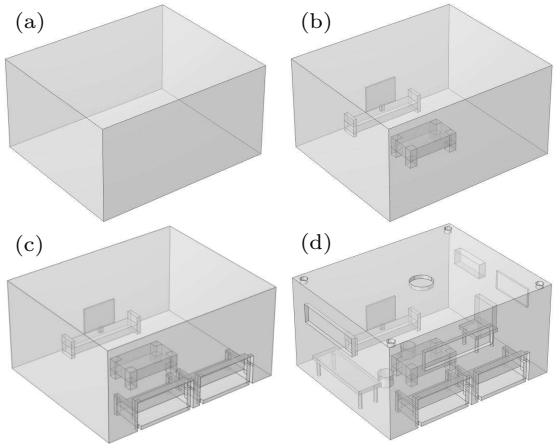


Fig. 1. Three-dimensional acoustic cavities with increasing interior complexity. (a) Empty cavity. (b) Cavity containing a television and a tea table. (c) Same as (b) but with two additional stools. (d) Same as (c) but further including an air conditioner, wall decorations, and additional tables, resulting in a more cluttered interior.

The acoustic pressure field $p(\boldsymbol{r})$ inside each cavity satisfies the three-dimensional Helmholtz equation,

$$\nabla^2 p + k^2 p = 0, \tag{1}$$

where $k = \omega/c$ is the acoustic wavenumber and $c = 343$ m/s is the speed of sound in air. Rigid (acoustically hard) boundary conditions are imposed on all walls,

$$\frac{\partial p}{\partial n} = 0, \tag{2}$$

which correspond to Neumann conditions implying zero normal particle velocity at the boundaries. This assumption is well justified for hard-walled acoustic enclosures where wall motion is negligible compared with the acoustic field.[26,27] This choice ensures a Hermitian eigenvalue problem with real eigenfrequencies and preserves time-reversal symmetry. Possible absorption or loss effects would render the system non-Hermitian and require a different statistical framework, which is not considered in the present work.

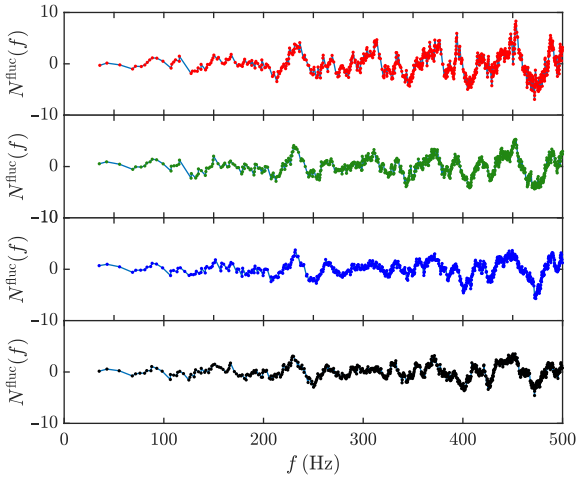


Fig. 2. Fluctuating part of the cumulative level number, $N_{\mathrm{fluc}}(f)$, as a function of frequency f for the four cavity models. The results for models (a)–(d) are shown from top to bottom.

Moreover, it allows the acoustic problem to be mapped onto a wave-chaotic analog of a closed quantum billiard, preserving time-reversal symmetry and energy conservation while avoiding the additional complexity of lossy or impedance-type boundaries. Such an approximation is widely adopted in wave-chaos studies, where the Helmholtz equation plays the same mathematical role as the Schrödinger equation in quantum systems.[4] Because of the irregular three-dimensional geometry, analytical or mode-matching approaches are intractable. Therefore, the eigenfrequencies and eigenmodes are computed numerically using the finite-element method (FEM) implemented in COMSOL MULTIPHYSICS. A sufficiently fine tetrahedral mesh is employed to ensure convergence, typically with at least ten elements per acoustic wavelength at the highest frequency considered (500 Hz). The resulting eigenvalue problem yields discrete resonance frequencies f_n and the corresponding pressure eigenfields $p_n(\boldsymbol{r})$. For each geometry, all eigenfrequencies within the range 50–500 Hz are extracted, providing several hundred modes for subsequent spectral and spatial analyses.

To minimize numerical artifacts, each eigenmode is checked for spatial continuity, and nearly degenerate pairs are treated as single levels. This preprocessing guarantees the completeness and reliability of the numerical spectra prior to unfolding and statistical evaluation.

Before conducting statistical analysis, the eigenfrequency spectra obtained from the four cavity geometries were first examined for completeness. The cumulative number of modes below a given frequency f can be expressed as

$$N(f) = N_{\text{fit}}(f) + N_{\text{fluc}}(f), \tag{3}$$

where $N_{\text{fit}}(f)$ represents the smooth part of the spectrum determined by Weyl's law, and $N_{\text{fluc}}(f)$ denotes the fluctuating component.[1,28]

Figure 2 shows the fluctuating part $N_{\text{fluc}}(f)$ as a function of frequency for models (a)–(d). The fluctuations remain bounded and oscillate around zero without systematic drift, confirming that the computed spectra are complete within the frequency range 50–500 Hz. Within this range, the total numbers of eigenfrequencies obtained for models (a)–(d) are 766, 775, 797, and 782, respectively. Additional numerical checks confirm that both short- and long-range spectral statistics extracted from these complete spectra are insensitive to further mesh refinement within the adopted discretization. This verification ensures that the subsequent statistical analyses are free from missing-level effects or unfolding bias. To characterize short-range spectral correlations, we computed the adjacent level-spacing ratio defined by

$$r_n = \frac{\min(\Delta_n, \Delta_{n+1})}{\max(\Delta_n, \Delta_{n+1})}, \tag{4}$$

where $\Delta_n = f_{n+1} - f_n$ represents the spacing between consecutive eigenfrequencies. In the integrable rectangular cavity, exact degeneracies arise due to geometric symmetries. Since the definition of the adjacent spacing ratio in Eq. (4) requires strictly ordered nonzero level spacings, each group of exactly degenerate eigenvalues is represented by a single eigenfrequency when evaluating $\langle r \rangle$. For non-integrable geometries, level repulsion suppresses degeneracies, and no special treatment is required.

Unlike the conventional nearest-neighbor spacing distribution, the ratio r_n does not require spectral unfolding and is therefore more robust against local density variations. Its ensemble average, $\langle r \rangle$, serves as a universal indicator distinguishing between regular and chaotic spectral statistics. The theoretical expectations are $\langle r \rangle_{\text{Poisson}} \approx 0.386$ for uncorrelated spectra and $\langle r \rangle_{\text{GOE}} \approx 0.536$ for chaotic spectra described by the GOE.[29,30] Figure 3 presents the calculated mean spacing ratios $\langle r \rangle$ for cavity models (a)–(d). The horizontal dashed lines mark the theoretical limits for the Poisson and GOE ensembles, while the blue solid line represents the numerical results from the acoustic simulations. A clear monotonic increase of $\langle r \rangle$ is observed as the cavity geometry becomes more irregular, indicating a gradual transition from uncorrelated (regular) spectra to the universal GOE regime. This trend reflects the onset of wave chaos induced by the increasing geometric complexity of the three-dimensional cavities.

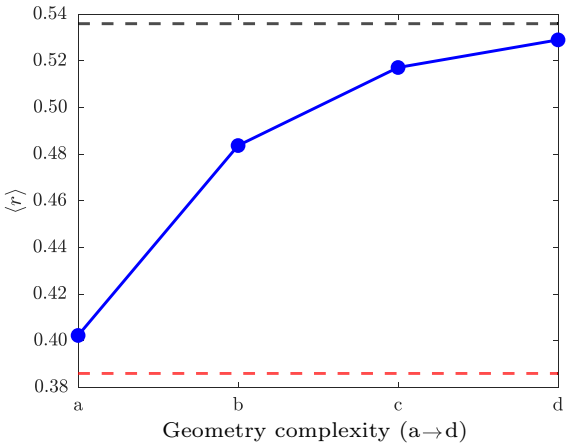


Fig. 3. Average adjacent level-spacing ratio $\langle r \rangle$ as a function of geometric complexity (a→d). The blue line with dots shows the simulated results obtained directly from the raw eigenvalue spectra without unfolding. The red and black dashed horizontal lines denote the theoretical predictions for Poisson and GOE statistics, $\langle r \rangle_{\text{Poisson}} \approx 0.386$ and $\langle r \rangle_{\text{GOE}} \approx 0.536$, respectively.

3. Spectral statistics and transition analysis

To provide a comprehensive statistical characterization of the acoustic eigenfrequency spectra, both short- and long-range correlations were analyzed using several complementary measures, as summarized in Fig. 4. The top-left panel shows the nearest-neighbor spacing distribution $P(s)$. For the Poisson and GOE ensembles,[31] the theoretical expressions are

$$P_{\text{P}}(s) = \mathrm{e}^{-s}, \quad P_{\text{GOE}}(s) = \frac{\pi s}{2} \exp\left(-\frac{\pi s^2}{4}\right). \tag{5}$$

The top-right panel presents the corresponding cumulative distribution,[32]

$$I(s) = \int_0^s P(s')\,\mathrm{d}s', \tag{6}$$

which smooths local fluctuations and emphasizes deviations at small spacings. The inset enlarges the region $1.8 \le s \le 3$, where subtle differences between models remain visible.

The bottom-left and bottom-right panels display the number variance $\Sigma^2(L)$ and the spectral rigidity $\Delta_3(L)$, which characterize long-range correlations in the unfolded spectra.[33] The number variance is defined as the mean-square deviation of the level-counting function $N(E)$ from its average over an interval of length L,

$$\Sigma^2(L) = \left\langle [N(E_0 + L) - N(E_0) - L]^2 \right\rangle_{E_0}, \tag{7}$$

where the brackets denote averaging over all starting positions E_0. The spectral rigidity $\Delta_3(L)$[34,35] measures the least-square

deviation of $N(E)$ from the best-fitting straight line within the same interval,

$$\Delta_3(L) = \left\langle \min_{A,B} \frac{1}{L} \int_{E_0}^{E_0+L} [N(E) - AE - B]^2 \, \mathrm{d}E \right\rangle_{E_0}. \quad (8)$$

Both quantities probe the degree of spectral stiffness: for Poisson statistics they increase linearly with L, whereas for GOE spectra they rise logarithmically, reflecting stronger level repulsion and correlations.

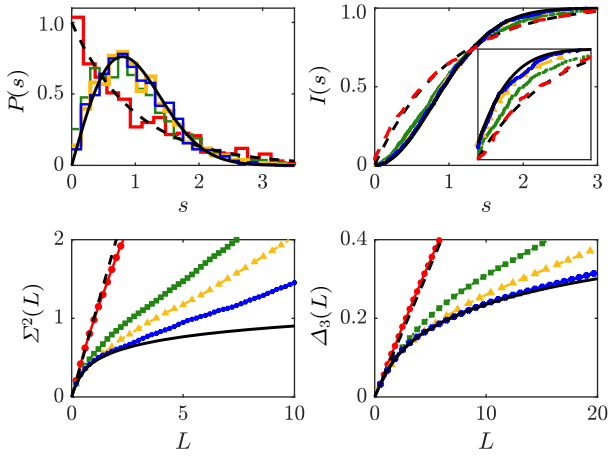


Fig. 4. Spectral statistics of the four cavity models. Shown are the nearest-neighbor spacing distribution $P(s)$ (top left), the cumulative distribution $I(s)$ (top right, with an inset showing the magnified region $1.8 \le s \le 3$), the number variance $\Sigma^2(L)$ (bottom left), and the spectral rigidity $\Delta_3(L)$ (bottom right). The red, green, yellow, and blue curves correspond to models (a)–(d), respectively. The black dashed and solid lines indicate the Poisson and GOE predictions, respectively.

Figure 4 shows the red, green, yellow, and blue curves corresponding to models (a)–(d), respectively. A systematic evolution is evident across all four measures — $P(s)$, $I(s)$, $\Sigma^2(L)$, and $\Delta_3(L)$ — showing a continuous transition from uncorrelated (Poisson-like) to correlated (GOE-like) statistics as the cavity geometry becomes more complex. The simplest configuration [model (a)] exhibits nearly uncorrelated spectra consistent with integrable dynamics, whereas the most irregular cavity [model (d)] shows strong spectral correlations approaching the GOE prediction. A small deviation remains visible in $\Sigma^2(L)$, which is known to be particularly sensitive to short periodic orbits that induce additional long-range correlations and slow convergence to the universal GOE limit.[23,36,37] Once these periodic contributions are effectively suppressed, the number variance follows the GOE curve much more closely (see Appendix A). Both short- and long-range spectral correlations thus exhibit a consistent trend toward GOE behavior from models (a) to (d), demonstrating that increasing geometric complexity enhances the level of wave chaos in the system.

To interpret these trends quantitatively, the intermediate regimes between uncorrelated and correlated spectra were analyzed using the BR model.[24,38,39] In this framework, the spectrum is modeled as a superposition of two statistically independent subsequences: a regular (Poisson-like) component with fractional weight ρ and a chaotic (GOE-like) component with fraction $\rho_c = 1 - \rho$. Using the Wigner-surmise approximation for the GOE part, the BR nearest-neighbor spacing distribution is given by

$$P_{\mathrm{BR}}(s;\rho) = \rho^2 \mathrm{e}^{-\rho s} \operatorname{erfc}\left(\tfrac{\sqrt{\pi}}{2}\rho_c s\right) + \left(2\rho\rho_c + \tfrac{\pi}{2}\rho_c^3 s\right) \mathrm{e}^{-\rho s - \frac{\pi}{4}\rho_c^2 s^2}. \quad (9)$$

This expression correctly reproduces the Poisson limit $P(s) = \mathrm{e}^{-s}$ for $\rho = 1$ and the GOE Wigner surmise $P(s) = \frac{\pi}{2} s \mathrm{e}^{-\pi s^2/4}$ for $\rho = 0$.

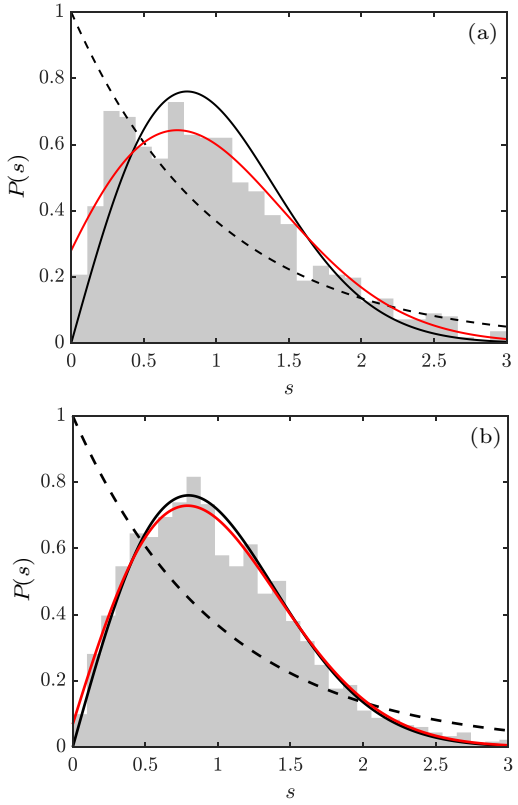


Fig. 5. Nearest-neighbor spacing distribution $P(s)$ for two cavity models. Panel (a) shows the result for model (b), and panel (b) for model (c). The histograms represent the numerical results, while the red curves show the best fits to the BR distribution, with $\rho = 0.152$ for model (b) and $\rho = 0.035$ for model (c). The black dashed and solid lines correspond to the Poisson and GOE predictions, respectively, as in Fig. 4.

For each model, the spacings were computed from the unfolded spectra and normalized to unit mean. The histograms in Fig. 5 (gray bars) were constructed over the frequency interval 50–500 Hz, and the parameter ρ was obtained by least-squares fitting of Eq. (9) to the numerical data. Panels (a) and (b) show the results for models (b) and (c), respectively. The red curves represent the best BR fits, yielding $\rho = 0.152$ for model (b) and $\rho = 0.035$ for model (c). The BR model provides a compact quantitative measure of the relative phase-space composition: the smaller the fitted parameter ρ, the larger the fraction of chaotic dynamics in the system. Accordingly, the obtained

values indicate that model (c) exhibits stronger spectral mixing and a higher degree of wave chaos than model (b). This behavior is fully consistent with the results shown in Fig. 4, where both short- and long-range spectral statistics evolve monotonically from Poisson-like toward GOE-like behavior as the cavity geometry becomes more complex.

In addition to the BR model, the spectral transition can also be described by the Brody distribution, which interpolates smoothly between the Poisson and GOE limits through a single empirical parameter β. While the BR model provides a physically motivated decomposition of regular and chaotic components, the Brody distribution[40] offers a phenomenological yet highly practical description of intermediate statistics when the underlying phase-space structure is not strictly separable.[6,25,41] A detailed comparison and fitting analysis based on the Brody model are presented in Appendix B.

4. Spatial statistics of acoustic modes

To elucidate the emergence of wave chaos in three dimensions, Fig. 6 displays the normalized spatial maps of $|p|$ for cavities of increasing complexity. Across geometries (top to bottom), the patterns evolve from symmetry-aligned, standing-wave-like structures to highly irregular, speckle-like fields. This evolution reflects progressive symmetry breaking and enhanced modal mixing: eigenmodes gradually lose separability and develop increasingly random spatial features, signaling a transition from integrable to chaotic dynamics.

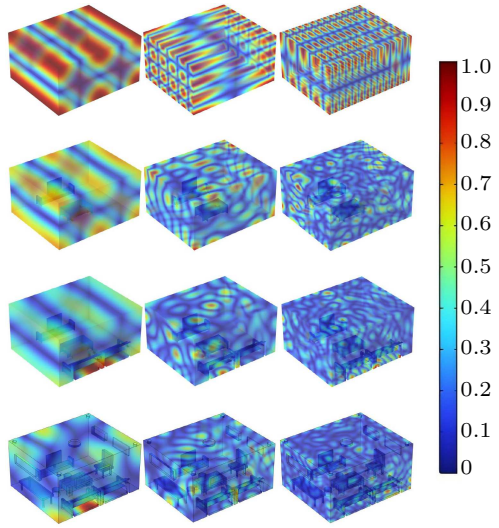


Fig. 6. Normalized spatial distributions of the acoustic pressure amplitude $|p|$ in three-dimensional cavities with increasing geometric complexity (a→d). Each row corresponds to one geometry, from top to bottom representing cases (a)–(d). For each geometry, three representative eigenmodes at (99.12, 299.49, 500.18) Hz for case (a), (99.28, 299.98, 500.40) Hz for case (b), (98.73, 299.73, 499.88) Hz for case (c), and (106.52, 300.07, 500.07) Hz for case (d) are shown from left to right. The color scale encodes the normalized pressure amplitude, with red and blue denoting the maximum and minimum values, respectively.

Within each geometry (left to right), the mode structure becomes more intricate with increasing frequency. At low frequencies, nodal sets remain nearly regular and aligned with cavity symmetries, whereas at higher frequencies, multiple scattering and boundary interference generate speckle-like intensity textures. The frequency-dependent increase in spatial randomness shows that, even for fixed geometry, higher excitation energies lead to denser spectra and stronger manifestations of wave chaos — consistent with the semiclassical picture in which complex classical trajectories dominate at higher energies.

To quantify these observations, we analyze the probability density $P(\psi)$ of the normalized amplitudes $\psi = p/\sqrt{\langle |p|^2 \rangle}$ for the four geometries in Fig. 1. For each geometry, forty eigenmodes centered around $f \approx 300$ Hz are selected, and approximately 8×10^5 spatial samples per mode are used to ensure statistical convergence; the normalized data are then pooled within each cavity.

In systems with fully developed wave chaos, real-valued amplitudes follow the Gaussian prediction,[12,42,43]

$$P_{\mathrm{G}}(\psi) = \frac{1}{\sqrt{2\pi}} \exp\left(-\frac{\psi^2}{2}\right), \tag{10}$$

which corresponds to a random superposition of plane waves with uncorrelated phases and directions. Deviations from this limit diagnose residual regularity: an enhanced central peak or suppressed tails typically indicate nonchaotic or mixed dynamics.

Figure 7 shows $P(\psi)$ for geometries (a)–(d) (colored curves) together with the Gaussian reference in Eq. (10) (black). As geometric complexity increases from (a) to (d), the amplitude statistics approach the Gaussian limit, indicating a gradual transition from regular to chaotic wave dynamics. The inset magnifies the neighborhood of $\psi = 0$, highlighting the evolution of the central peak. Taken together with the morphology in Fig. 6, these results demonstrate that both field patterns and local amplitude statistics consistently capture the onset and strengthening of wave chaos in increasingly complex cavity geometries.

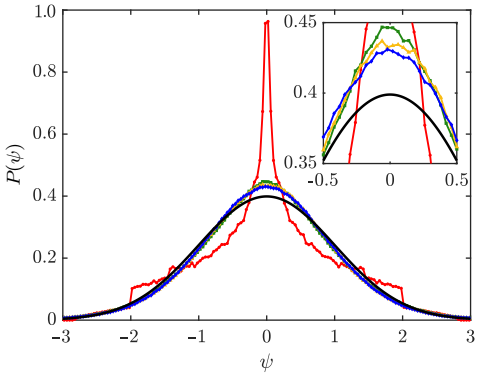


Fig. 7. Probability density $P(\psi)$ of normalized amplitudes for the four cavity geometries (a→d). The red, green, yellow, and blue curves correspond to cases (a)–(d), respectively; the black solid line is the Gaussian prediction. The inset enlarges the region near $\psi = 0$ for clarity.

5. Conclusion

In summary, we have performed a systematic numerical investigation of the transition from regular to chaotic wave dynamics in three-dimensional acoustic cavities with progressively increased geometric complexity. Large ensembles of eigenfrequencies and eigenmodes were computed and analyzed through complementary spectral and spatial statistics. The unfolded level sequences exhibit a continuous evolution from Poisson to GOE statistics, confirming the onset of chaotic behavior in the acoustic spectra.

In the integrable rectangular cavity, acoustic modes are separable and characterized by well-defined quantum numbers, leading to regular nodal patterns and the absence of mode coupling. As geometric complexity increases, separability is progressively destroyed and waves undergo repeated multipath scattering from irregular boundaries. This induces strong coupling between modes with different spatial structures, resulting in hybridized eigenfunctions that extend throughout the cavity. From a semiclassical perspective, this mode mixing reflects the transition of the underlying ray dynamics from regular to chaotic motion, which directly manifests itself in the observed crossover of spectral statistics from Poisson to GOE behavior.

This transition was quantitatively captured by the BR and Brody interpolations, which yield consistent estimates of the degree of chaotic mixing. The corresponding spatial mode patterns display a clear morphological evolution — from symmetry-aligned standing waves to highly irregular speckle-like fields — indicating the progressive loss of separability and the emergence of strong mode mixing. Moreover, the probability density of the normalized wavefunction amplitudes approaches the Gaussian prediction as the structure becomes more complex, in full agreement with the expectations for fully developed wave chaos.

Overall, these results demonstrate a robust correspondence between geometric irregularity and the statistical indicators of chaos in both spectral and spatial domains. They establish three-dimensional acoustic resonators as controllable and experimentally realizable analog platforms for exploring the universal features of wave and quantum chaos and for elucidating how geometry and symmetry breaking shape the onset of statistical universality in complex wave systems. The observed spectral transition reflects the universal distinction between integrable and chaotic wave systems with time-reversal symmetry and does not rely on specific geometric realizations.

Appendix A: Numerical procedure for removing periodic-orbit contributions

To elucidate the influence of short periodic orbits on the fluctuation statistics and to demonstrate the numerical procedure used for their suppression, we analyze in detail the unfolded spectrum of model (d). Using the definition of the fluctuating part $N_{\mathrm{fluc}}(f)$ introduced in Eq. (3),

We compute its Fourier transform with respect to the wavenumber $k = 2\pi f/c$, which yields the so-called length spectrum,[23,43,44]

$$P(L) = \left| \int N_{\mathrm{fluc}}(k)\, \mathrm{e}^{2\mathrm{i}kL}\, \mathrm{d}k \right|^2, \tag{A1}$$

where peaks in $P(L)$ correspond to dominant classical periodic orbits of length L. This semiclassical correspondence enables the identification and subsequent removal of nonuniversal, orbit-related contributions from the spectral fluctuations.

Figure A1 displays $N_{\mathrm{fluc}}(N)$ as a function of the unfolded level index. The black curve represents the raw fluctuation sequence, which exhibits rapid oscillations around zero, whereas the red curve denotes the smoothed background obtained by low-pass filtering with a finite window size. This slowly varying component reflects the cumulative effect of short periodic orbits and other nonuniversal structures. By subtracting the red curve from the raw data, we isolate the residual fluctuation sequence that more faithfully captures the universal random-matrix-type correlations.

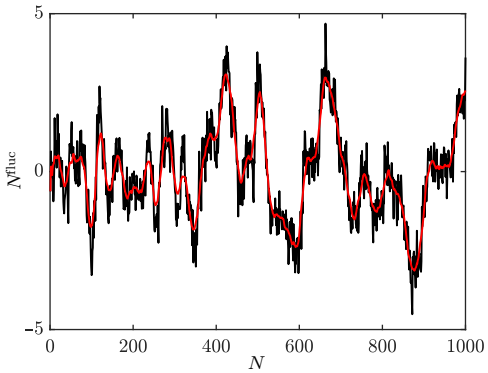


Fig. A1. Fluctuating part of the cumulative level number $N_{\mathrm{fluc}}(N)$ as a function of the unfolded level index N for model (d). The black curve shows the raw fluctuation data, while the red curve represents the smoothed component obtained by low-pass filtering.

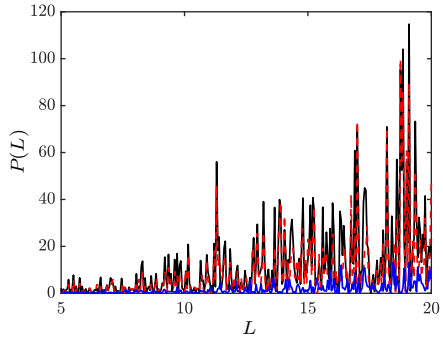


Fig. A2. Length spectrum $P(L)$ calculated from the fluctuation part of the cumulative level number N_{fluc} for model (d). The black curve corresponds to the spectrum obtained from the raw fluctuations, the red curve from the smoothed component, and the blue curve from the corrected fluctuations after subtraction of the smooth background.

The corresponding length spectrum $P(L)$ is shown in Fig. A2. The strong peaks in the black and red curves correspond to dominant periodic orbits whose lengths match the characteristic dimensions of the cavity. After removing the smoothed component (blue curve), these orbit-related peaks are strongly suppressed, and the remaining spectrum becomes smoother and less structured, as expected when nonuniversal semiclassical effects are eliminated. This demonstrates that the subtraction procedure effectively isolates the stochastic component of the spectrum associated with wave chaos.

Finally, Fig. A3 shows the number variance $\Sigma^2(L)$ calculated from the corrected unfolded spectrum after removal of the smooth background. The blue curve follows the GOE prediction (black solid line) closely across the entire range of L, in sharp contrast to the uncorrected case, where residual deviations persist at large L. The suppression of long-range drift indicates that the orbit-induced oscillations — previously responsible for the excess variance — have been effectively eliminated.[45,46]

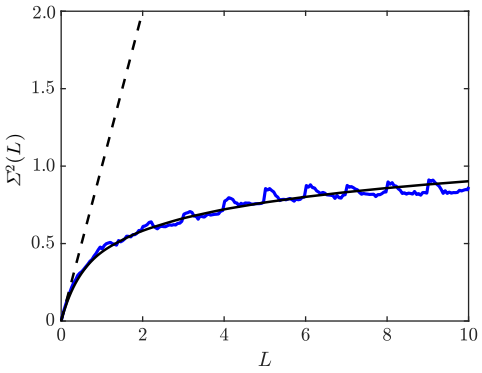


Fig. A3. Number variance $\Sigma^2(L)$ as a function of interval length L for model (d). The blue curve shows the numerical result calculated from the unfolded spectrum after subtracting the smoothed component of N_{fluc} (see Fig. A1). The black solid line denotes the GOE prediction, and the black dashed line corresponds to the Poisson prediction.

These results confirm that the combined low-pass filtering and subtraction scheme provides a robust and systematic numerical method for eliminating short-periodic-orbit effects and recovering the universal spectral correlations predicted by random-matrix theory. This procedure establishes a reliable bridge between semiclassical orbit dynamics and statistical universality in chaotic acoustic cavities.

Appendix B: Brody distribution analysis and comparison

To further characterize the spectral statistics within an alternative theoretical framework, the Brody distribution was employed to fit the nearest-neighbor spacing distributions of models (b) and (c). The Brody form provides an empirical single-parameter interpolation between the Poisson and GOE limits and is defined as

$$P_{\text{B}}(s;\beta) = A(\beta+1)s^{\beta}\exp[-As^{\beta+1}], \tag{11}$$

$$A = \left[\Gamma\left(\frac{\beta+2}{\beta+1}\right)\right]^{\beta+1}, \tag{12}$$

where s denotes the nearest-neighbor spacing and β is the Brody parameter that continuously evolves from $\beta = 0$ (Poisson limit) to $\beta = 1$ (GOE limit).[6] The parameter β thus serves as a compact quantitative indicator of spectral correlations and can be regarded as a phenomenological measure of the transition from integrable to chaotic dynamics.

Figure B1 compares the numerical spacing distributions with the Brody fits. The extracted parameters $\beta = 0.583$ for model (b) and $\beta = 0.879$ for model (c) indicate that the degree of spectral correlation increases with the geometric complexity of the cavity. The fitted curves smoothly interpolate between the uncorrelated Poisson and fully correlated GOE limits, demonstrating that the Brody parameter provides a consistent quantitative description of the transition. These results are in excellent agreement with the BR analysis presented in the main text, reinforcing the conclusion that increasing structural complexity drives the system toward chaotic spectral behavior.

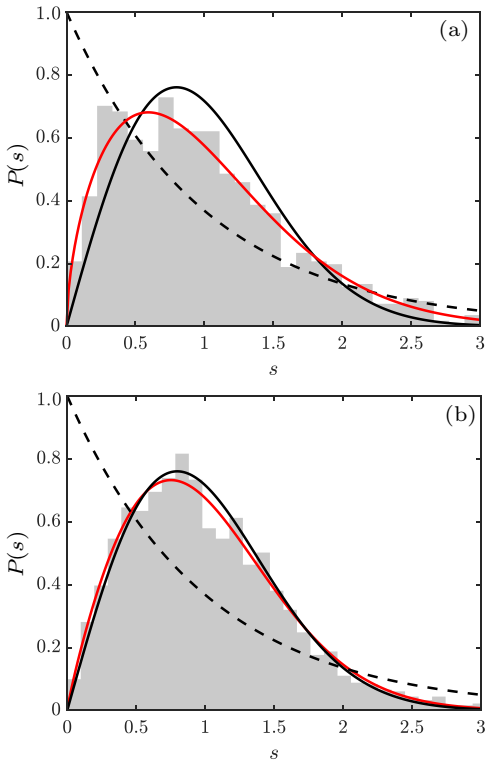


Fig. B1. Nearest-neighbor spacing distributions $P(s)$ of model (b) [panel (a)] and model (c) [panel (b)] fitted with the Brody distribution. The gray histograms represent the numerical data, while the red curves show the best Brody fits with $\beta = 0.583$ for model (b) and $\beta = 0.879$ for model (c). The black dashed and solid lines denote the Poisson and GOE predictions, respectively.

Acknowledgements

This work was supported by the National Natural Science Foundation of China (Grant Nos. 11775100, 12247101, and 11961131009), the Fundamental Research Funds for the Central Universities (Grant No. lzujbky-2025-jdzx07),

the Natural Science Foundation of Gansu Province (Grant Nos. 22JR5RA389 and 25JRRA799), and the '111 Center' under Grant No. B20063. X.Z. acknowledges financial support from the China Scholarship Council (Grant No. CSC-202306180087).

References

[1] Stöckmann H J 1999 *Quantum Chaos: An Introduction* (Cambridge: Cambridge University Press)
[2] Bohigas O, Giannoni M J and Schmit C 1984 *Phys. Rev. Lett.* **52** 1
[3] Stöckmann H J 2013 *Chaos in Microwave Resonators* (Basel: Springer Basel)
[4] Alt H, Dembowski C, Gräf H D, Hofferbert R, Rehfeld H, Richter A, Schuhmann R and Weiland T 1997 *Phys. Rev. Lett.* **79** 1026
[5] Mehta M L 2004 *Random Matrices* (Amsterdam: Elsevier)
[6] Brody T A, Flores J, French J B, Mello P A, Pandey A and Wong S S M 1981 *Rev. Mod. Phys.* **53** 385
[7] Haake F 1991 *Quantum Signatures of Chaos* (Boston: Springer US)
[8] Sieber M, Primack H, Smilansky U, Ussishkin I and Schanz H 1995 *J. Phys. A: Math. Gen.* **28** 5041
[9] Schierenberg S, Bruckmann F and Wettig T 2012 *Phys. Rev. E* **85** 061130
[10] Zhang X, Che J and Dietz B 2024 *Chin. Phys. B* **33** 120501
[11] Zhang R, Zhang W, Dietz B, Chai G and Huang L 2019 *Chin. Phys. B* **28** 100502
[12] Stöckmann H J and Stein J 1990 *Phys. Rev. Lett.* **64** 2215
[13] Białous M, Dietz B and Sirko L 2020 *Phys. Rev. E* **102** 042206
[14] Ellegaard C, Guhr T, Lindemann K, Lorensen H Q, Nygård J and Oxborrow M 1995 *Phys. Rev. Lett.* **75** 1546
[15] Sinai Y G 1970 *Russ. Math. Surv.* **25** 137
[16] Białous M, Dietz B and Sirko L 2023 *Phys. Rev. E* **107** 054210
[17] Zhang X, Zhang W, Che J and Dietz B 2023 *Phys. Rev. E* **108** 044211
[18] Dietz B and Richter A 2015 *Chaos* **25** 097601
[19] Stoffregen U, Stein J, Stöckmann H J, Kuś M and Haake F 1995 *Phys. Rev. Lett.* **74** 2666
[20] Sridhar S 1991 *Phys. Rev. Lett.* **67** 785
[21] Tanner G and Søndergaard N 2007 *J. Phys. A: Math. Theor.* **40** R443
[22] Zhao D, Ji C and Yin M 2022 *Aerosp. Sci. Technol.* **128** 107799
[23] Heusler S, Müller S, Altland A, Braun P and Haake F 2007 *Phys. Rev. Lett.* **98** 044103
[24] Berry M V and Robnik M 1984 *J. Phys. A: Math. Gen.* **17** 2413
[25] Manos T and Robnik M 2013 *Phys. Rev. E* **87** 062905
[26] Kinsler L E, Frey A R and Bennett G S 1951 *Am. J. Phys.* **19** 254
[27] Pierce A D 1989 *Acoustics: An Introduction to Its Physical Principles and Applications* 2nd ed (Woodbury, NY: Acoustical Society of America)
[28] Weyl H 1911 *Nachrichten von der Gesellschaft der Wissenschaften zu Göttingen, Mathematisch-Physikalische Klasse* **1911** 110
[29] Atas Y Y, Bogomolny E, Giraud O and Roux G 2013 *Phys. Rev. Lett.* **110** 084101
[30] Oganesyan V and Huse D A 2007 *Phys. Rev. B* **75** 155111
[31] Weidenmüller H A and Mitchell G E 2009 *Rev. Mod. Phys.* **81** 539
[32] Abul-Magd A Y and Simbel M H 1999 *Phys. Rev. E* **60** 5371
[33] Ossipov A, Rushkin I and Cuevas E 2012 *Phys. Rev. E* **85** 021127
[34] Georgopulos P D and Camarda H S 1981 *Phys. Rev. C* **24** 420
[35] Mulhall D 2009 *Phys. Rev. C* **80** 034612
[36] Dietz B, Mößner B, Papenbrock T, Reif U and Richter A 2008 *Phys. Rev. E* **77** 046221
[37] Gräf H D, Harney H L, Lengeler H, Lewenkopf C H, Rangacharyulu C, Richter A, Schardt P and Weidenmüller H A 1992 *Phys. Rev. Lett.* **69** 1296
[38] Makino H and Tasaki S 2003 *Phys. Rev. E* **67** 066205
[39] Rudolf T, Mertig N, Löck S and Bäcker A 2012 *Phys. Rev. E* **85** 036213
[40] Brody T A 1973 *Lett. Nuovo Cimento* **7** 482
[41] Bäcker A, Ketzmerick R, Löck S and Mertig N 2011 *Phys. Rev. Lett.* **106** 024101
[42] Berry M V 1977 *J. Phys. A: Math. Gen.* **10** 2083
[43] Dietz B, Mößner B, Papenbrock T, Reif U and Richter A 2008 *Phys. Rev. E* **77** 046221
[44] Laurent D, Legrand O and Mortessagne F 2006 *Phys. Rev. E* **74** 046219
[45] Zhang W, Zhang X and Dietz B 2024 *Eur. Phys. J. Spec. Top.* **233** 1275
[46] Dietz B, Yunko V, Białous M, Bauch S, Ławniczak M and Sirko L 2017 *Phys. Rev. E* **95** 052202